Coherent Vibrational Dynamics in an Isolated Peptide Captured with 2D IR Spectroscopy

Zifan Ma,[a] Laura M. McCaslin,[b] and Joseph A. Fournier[a]*

[a]Department of Chemistry, Washington University in St. Louis, St. Louis, MO 63130

[b]Sandia National Laboratories, Livermore, CA 94550

*corresponding author: jfournier@wustl.edu

Abstract

Quantum mechanical vibrational coherence transfer processes play important roles in energy relaxation, charge transfer, and reaction dynamics in chemical and biological systems, but are difficult to directly measure using traditional condensed-phase nonlinear spectroscopies. Recently, we developed a new experimental capability to obtain two-dimensional infrared (2D IR) spectra of molecular systems in the gas phase that enables the direct measurement of coherence pathways. Herein, we report ultrafast 2D IR spectroscopy of the peptide glutathione (GSH) isolated and cryogenically cooled in the gas phase. Six vibrational modes were simultaneously excited within the amide I and II region. The spectral dynamics of both diagonal and off-diagonal cross peak features exhibit long-lived oscillatory behavior consistent with the presence of coherent vibrational dynamics. The oscillatory signatures deviate significantly from the expected quantum beating pathways predicted from standard nonlinear response theories. These deviations indicate the presence of additional nonlinear pathways, including coherence transfer processes. Quantum chemistry calculations indicate large anharmonic couplings between the excited vibrational modes in GSH and, critically, strong coupling between the excited modes and numerous low-frequency modes that act as a bath to mediate coherence transfer. The data provide important new benchmarks for modeling coherence transfer dynamics and system-bath interactions in open quantum systems free from solvent effects.

Introduction

Coherent multidimensional spectroscopies, such as two-dimensional electronic and two-dimensional infrared (2D IR), have become valuable experimental methods for the study of energy relaxation dynamics, charge transfer reactions, solute-solvent interactions, and anharmonic coupling with molecular-level specificity.[1,2] Time-dependent perturbation theory has proven highly successful in describing the interaction pathways between the system and laser fields that give rise to diagonal and off-diagonal cross peak features in 2D spectra through nonlinear response functions.[3–6] Perturbative approaches that assume weak system-bath interactions can accurately model the time evolution and energy relaxation dynamics of excited molecular systems.[7–10]

Transient and 2D IR spectroscopies have been extensively utilized to study vibrational relaxation dynamics in a wide range of molecular and biological systems.[11–20] These experiments can track energy flow from an initially excited chromophore group to other regions of the molecular system in a site-specific fashion. In model peptides, vibrational relaxation dynamics have been found to be mediated by the peptide backbone in α-helix systems,[14] while relaxation in β-sheets was observed to occur through the hydrogen bond network.[16] In both of these studies, the timescales were competitive between intramolecular relaxation pathways and intermolecular relaxation to the solvent. Vibrational relaxation in these studies was modeled with classical molecular dynamics simulations, providing qualitative agreement with the experimental dynamics.[14,16] Closer theoretical and experimental agreement has been achieved through the application of quantum scaling factors to the classical dynamics, correcting for quantum effects such as zero-point energy.[21]

Two interaction pathways involving quantum mechanical coherences are quantum beating and coherence transfer. In quantum beating pathways, the pump pulse bandwidth is sufficiently large to excite a superposition between two states. The excited superposition state gives rise to an oscillatory signal during the pump-probe delay time that evolves at the difference frequency between the states.[22,23] A second class of pathways involve coherence transfer, where a phase relationship from an initially excited coherent superposition between two states is transferred to a coherence between two other states. Coherence transfer can be spectroscopically identified when quantum beating signals contain additional frequency components arising from the superposition states involved in the transfer.[24] Other processes such as coherence-to-population and population-to-coherence transfer processes have also been suggested.[25,26] Coherence transfer processes have been proposed as important mediators in charge transfer reactions in photosynthetic light harvesting systems[27–35] and optoelectronic materials.[36–38] Maintaining coherent relationships is a key challenge in quantum computing and information sciences.[39–41] However, direct spectroscopic measurements of coherence transfer remains a grand experimental challenge. This experimental difficulty arises because oscillatory quantum beating signals are often washed out by the exponential decay dynamics from population relaxation, population transfer, and dephasing. Consequently, coherence transfer is typically neglected in data analysis and computational modeling, a simplification known as the secular approximation in nonlinear response theories.[22,25]

Due to rapid population relaxation dynamics typically observed in condensed-phase systems, the oscillatory signatures of quantum beating pathways are often not observed above experimental signal-to-noise ratios. The identification of multiple quantum beating signals from coherence transfer pathways is even more difficult to measure. Consequently, there has been debate in the literature over how to assign spectroscopic signatures that exhibit coherence transfer pathways.[22,24,42,43] Vibrational coherence transfer was first suggested in the solution-phase rhodium dicarbonyl model system $Rh(CO)_2C_5H_7O_2$ by Khalil et al. through 2D IR experiments and theoretical modeling.[22] In the 2D IR spectrum, forbidden combination band transitions between the symmetric and antisymmetric carbonyl stretch modes were observed. The appearance of these forbidden transitions was posited to arise from multiple coherence transfer processes between the bright carbonyl stretch modes and the dark combination bands. Later 2D IR experiments on the same system by Marroux and Orr-Ewing tested this assignment by using narrowband pumping to eliminate superposition excitation of the symmetric and antisymmetric carbonyl stretches, therefore preventing quantum beating pathways.[43] These spectra exhibited the same forbidden transitions, which they assigned to rapid population relaxation dynamics between the symmetric and antisymmetric carbonyl stretches. Multiple theoretical modeling studies suggested that coherence transfer in $Rh(CO)_2C_5H_7O_2$ occurs on a timescale much longer than population relaxation.[25,43]

The first unambiguous measurements of vibrational coherence transfer using 2D IR were reported by Nee et al. in the metal carbonyl system $Mn_2(CO)_{10}$.[24] Coherence transfer was identified from the observation of multi-frequency quantum beating components in several off-diagonal cross peak features between the coupled carbonyl stretching modes. Similar oscillatory cross peak behavior consistent with coherence transfer was later observed by Eckert and Kubarych in a series of $[Fe(CO)_3]_2$ complexes.[44] Very recently, Guerrieri et al. reported vibrational coherence transfer between Fermi resonance coupled modes in the carbonyl stretch region of ethylene carbonate.[26] Oscillatory dynamics in the diagonal features that are not predicted from the standard secular interaction pathways in nonlinear response theories were an indication of coherence transfer processes.

To develop new insight into energy transfer and relaxation processes, spectroscopic experiments are needed that can differentiate the signatures of quantum beating and coherence transfer pathways from population relaxation pathways. Recently, we demonstrated the acquisition of transient and 2D IR spectra of gas phase, cryogenically cooled molecular ions.[45,46] These experiments enable the measurement of high-resolution 2D IR spectra of well-defined systems free from intermolecular solvent effects and dynamics. Our experiments employ an action-based detection approach, where modulations in photofragmentation of a weakly bound "messenger tag" molecule are used to measure the nonlinear response of the system. These experiments are insensitive to population relaxation and transfer dynamics, allowing for the isolation of quantum beating and coherence transfer pathways. Here, we report the 2D IR spectra of the protonated small peptide glutathione (GSH) spanning the amide I and II spectral regions. The measured dynamics

and amplitudes of both the diagonal and off-diagonal cross peak features deviate significantly from those predicted from the secular approximation to nonlinear response theories, indicating the presence of nonsecular pathways including coherence transfer. Quantum chemistry calculations reveal large cubic coupling constants between the excited vibrational modes and between excited and numerous low-frequency vibrations. These low-frequency vibrations act as a bath to mediate coherence transfer processes, providing important insight into system-bath coupling in open quantum systems.

Experimental and Computational Methods

Detailed descriptions of the WashU cryogenic ion photofragmentation mass spectrometer and ultrafast laser system have been previously reviewed.[47] Briefly, a 1 mM solution of GSH (Chem-Impex Int'l. Inc.) was prepared in acetonitrile with 0.1% formic acid. The GSH ions were generated with electrospray ionization and guided through three differentially pumped stages using RF-only hexapole ion guides. The ions were cryogenically cooled and stored in a 3D quadrupole Paul trap (Jordan TOF, Inc.), which is attached to the second-stage of a closed-cycle helium cryostat (Janis Research). The ions were initially confined within the first hexapole guide for a duration of 95 ms by applying a repulsive voltage to the exit aperture. A pulse valve (Parker Hannifin, Series 9 general valve) was activated 3 ms after the ions exited the first guide, ensuring synchronization of helium buffer gas with the ions' arrival into the ion trap. The ions were collisionally cooled at 28 K, leading to the formation of N_2-tagged complexes of GSH promoted by trace nitrogen in the helium buffer gas. The buffer gas burst had a duration of approximately 30 ms. A low-amplitude RF pulse between 30 and 40 ms was applied to sweep out untagged GSH ions from the trap. After sweeping, the tagged ions were irradiated, followed by extraction into a reflectron time-of-flight mass spectrometer. The ion signal was measured with a dual microchannel plate (MCP) detector.

Linear IR action spectra were recorded using a tunable infrared optical parametric oscillator/amplifier (OPO/OPA) system (LaserVision). The OPO/OPA system was pumped by a Nd:YAG laser (Continuum Surelite EX, 10 Hz, 7 ns pulse duration, 660 mJ per pulse) and the output was tunable across the 2000-4500 cm^{-1} range, with pulse energies varying between 2 and 40 mJ per pulse. The lower frequency range (600-2200 cm^{-1}, 0.1-1 mJ per pulse) was generated by difference frequency mixing of the OPA signal and idler beams in an $AgGaSe_2$ crystal. The resolution of the system is ~3 cm^{-1}. Action spectra were collected by recording the N_2 photodissociation yield as a function of the infrared frequency. The reported spectrum is from the average of 10 scans, with data binned at 1 cm^{-1} interval. The spectrum was normalized by dividing by the laser power at each frequency to account for variation in the laser power over the scanning range.

Ultrafast experiments were performed utilizing a Ti:Sapphire oscillator/regenerative amplifier laser system (Coherent Astrella, 800 nm, 1 kHz, 35 fs, 3.6 W). The 800 nm output

pumped a commercial OPA (Light Conversion, TOPAS Prime) to generate tunable near-infrared signal (1.2−1.7 μm) and idler (1.7−2.4 μm) pulses. The signal and idler beams were sent into a homebuilt difference frequency generation (DFG) system with a type I $AgGaS_2$ crystal to produce mid-infrared pulses centered at 1650 cm^{-1} (~ 32 μJ per pulse, ~200 cm^{-1} bandwidth, <100 fs pulse duration). The IR pulse was then sent into a mid-IR germanium acousto-optic modulator (AOM) pulse shaper (PhaseTech Spectroscopy) to generate pulse trains with precisely controlled amplitudes, time delays, and relative phases. For each 10 Hz cycle of the mass spectrometer, 100 identical pulse trains were directed into the ion trap and interactions between 40-95 ms were used to accumulate photoproduct intensity. The photodissociation yield for each pulse train was averaged over 16 mass spectrometer cycles. The N_2 photodissociation yield was recorded as a function of interpulse delays (τ_1, τ_2, τ_3). Further experimental details and data processing procedures are provided in Supporting Information (SI).

The minimum-energy structure of protonated GSH was found using the configurational search procedure outlined in SI. Harmonic calculations on the minimum-energy structure were performed at the ωB97X-D/6-31G(d) level and basis set using the ORCA software package.[48] To obtain the cubic force constants, anharmonic second-order vibrational perturbation theory (VPT2) calculations[49] were performed at the ωB97X-D/6-31G(d) level and basis set in Q-Chem 5.4.[50]

Results and Discussion

Structure and Vibrational Spectrum. The computed minimum-energy structure of protonated GSH is shown in Fig. 1a. The protonated terminal amine group results in a compact structure where hydrogen bonds are formed between the $–NH_3^+$ group and the four carbonyl groups. This structure is consistent with the calculated minimum-energy structure reported by Gregori et al.[51] The experimental and computed linear IR spectra in the amide I-II region are compared in Figs. 1b and 1c, respectively. The strongest feature near 1785 cm^{-1} results from the two overlapping carbonyl stretching modes of the terminal carboxylic acid groups. The remaining lower-energy transitions have more complicated normal mode displacements (Fig. S1) that each involve bending motions of the $–NH_3^+$ group. The pair of transitions near 1675 cm^{-1} involve carbonyl stretching of the cysteine and glycine residues and, therefore, are best characterized as the amide I modes. The strong transition at 1510 cm^{-1} mostly derives from NH bending of the cysteine residue while its weaker partner at 1540 cm^{-1} derives from NH bending of the glycine residue, consistent with amide II vibrations. The pair of transitions at 1469 cm^{-1} and 1608 cm^{-1} each mainly consist of $–NH_3^+$ bending motions. Importantly, the good agreement between experiment and theory indicates that the calculated minimum-energy structure is the only conformer present experimentally.

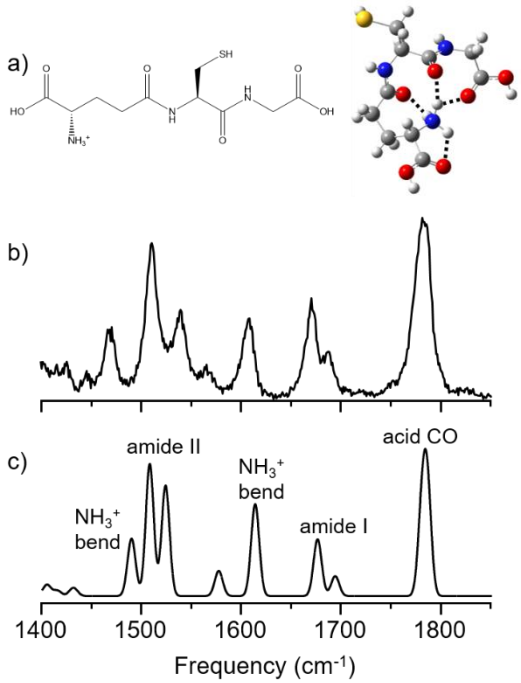

Fig. 1. (a) Minimum-energy structure of protonated GSH. (b) Linear vibrational action spectrum in the amide I-II region. (c) Calculated harmonic spectrum (ωB97X-D/6-31G(d), scaled by 0.944 to bring the high-energy carbonyl acid stretch into agreement with the experimental spectrum).

Action 2D IR Spectra. 2D IR spectra at pump-probe waiting times of 150 fs and 2000 fs are presented in Figs. 2a and 2b, respectively. Spectra collected at 500 fs and 1000 fs waiting times are provided in Fig. S2. Negative bleaching signals are observed along the diagonal (pump frequency ω_1 = probe frequency ω_3) for each of the six main transitions, labeled 1-6 in Fig. 2, within the bandwidth the laser pulses between 1425-1725 cm^{-1}. Weaker off-diagonal cross peak bleach features are also present between each pair of diagonal transitions.

Absent from the spectra are excited-state transitions that accompany each bleach feature, which are commonplace in traditional pump-probe and 2D spectroscopies. The absence of excited-state transitions is a consequence of the action-based scheme. In action-detection experiments, there is an additional probe pulse (four light-matter interactions overall) that is not present in traditional nonlinear experiments where there are three light-matter interactions.[45,52,53] The additional probe pulse introduces a new interaction pathway that corresponds to a bleaching signal of the excited states.[54] This new excited-state bleaching pathway destructively interferes with the positive excited-state absorption pathway, leading to the absence of positive features in the 2D action spectra. Feynman diagrams comparing traditional and action 2D IR interaction pathways are reviewed in SI. Importantly, the removal of excited-state features from action 2D IR

spectra reduces spectral congestion, enabling clearer assignment of oscillatory quantum beating and coherence transfer signatures compared to traditional 2D IR experiments.

In traditional 2D IR, the splitting between the bleach and excited-state transitions of off-diagonal cross peak features provide a measure of the anharmonic coupling between two modes. In the harmonic limit, the cross peak bleach and excited-state transitions occur at the same frequency and perfectly destructively interfere. This destructive interference between the bleach and excited-state pathways results in no cross peak signal, as expected for two uncoupled modes. For weakly coupled modes, the cross peak bleach and excite-state transitions are slightly separated in frequency, resulting in partial destructive interference and the appearance of a "weak" cross peak. With increased anharmonic coupling, the cross peak signals separate further to yield "strong" cross peak signals. Population transfer between modes increases the cross peak bleach/excited-state splitting, reducing the interference between the pathways and causing a "growth" in the cross peak signal with increasing pump-probe waiting time.[6,55] The growth of cross peak signals is used to measure population transfer dynamics between different vibrational modes.

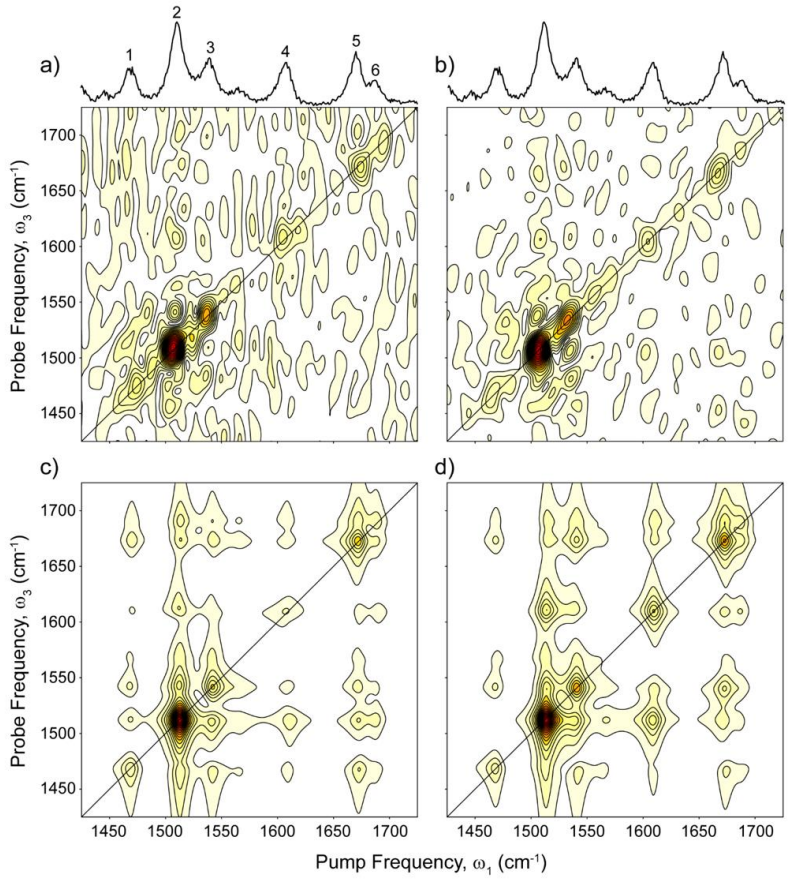

Fig. 2. Absolute value absorptive 2D IR action spectra of GSH at pump-probe waiting times of (a) 150 fs and (b) 2000 fs. The linear IR spectrum is shown at the top of each panel. Simulated 2D IR spectra under the secular approximation to nonlinear response theories at waiting times of (c) 150 fs and (d) 2000 fs (see main text and SI for simulation details).

While important molecular and dynamical information are lost in action 2D IR, the removal of overlapping positive and negative features allows for improved resolution and measurement of transitions within congested spectral regions. This is particularly evident in the 1450-1550 cm^{-1} region in GSH where the cross peak bleach features between modes 1, 2, and 3 are well resolved. Importantly, the elimination of interfering excited-state pathways means that cross peak bleach features are inherent in action 2D IR and do not derive from anharmonic coupling or population transfer dynamics. Population relaxation dynamics, which causes exponential decay of bleach features, will also be absent from diagonal and cross peak signals in the presented gas-phase measurements since there is no solvent to dissipate the excitation energy. Without intermolecular relaxation to solvent, the system cannot return to the overall ground vibrational state. Therefore, the exponential decay dynamics that usually mask quantum beating signatures in traditional 2D IR will be absent in gas-phase action experiments. As a result, spectral dynamics during the pump-probe waiting time will primarily derive from quantum beating pathways involving coherences. Note that loss of the N_2 messenger tag is expected to occur on much longer timescales and is not expected to influence the measured spectra or dynamics.[56–59]

Dynamics of Diagonal Features. The intensity of diagonal bleach features in both traditional and action 2D IR spectra scale as the transition dipole moment to the fourth power, $|\mu_{A0}|^4$, where μ_{A0} denotes the transition dipole moment of the fundamental (v = 0 to 1) for mode A. Nonlinear response pathways can be classified as either a "rephasing" pathway or a "nonrephasing" pathway. Rephasing and nonrephasing pathways differ by how the excited coherences evolve during the delay between the two pump pulses, τ_1, compared to during the delay between the two probe pulses, τ_3.[6] Each diagonal feature involving a single mode A has four contributing nonlinear pathways: rephasing ground-state bleach, nonrephasing ground-state bleach, rephasing stimulated emission, and nonrephasing stimulated emission.

When pathways involving pairs of modes are considered, additional nonrephasing signals occur along the diagonal. These signals arise from the pump pulses creating a coherent superposition state between two modes that fall within the bandwidth of the pulses.[6,22] These pathways result in quantum beating signals that oscillate at the difference frequency between the two excited modes during the pump-probe waiting time τ_2. Together, the signals from these one and two-mode pathways make up the complete set of components captured in the secular approximation to nonlinear response theories. These signals give rise to diagonal features at $(\omega_1, \omega_3) = (\omega_A, \omega_A)$ that evolve as:

$$\text{Signal}_A(\tau_2) \propto |\mu_{A0}|^4 + |\mu_{A0}|^2 \sum_j |\mu_{j0}|^2 e^{-i\omega_{Aj}\tau_2} \left(\frac{1}{15}\left(1 + 2\cos^2(\theta_{Aj})\right)\right) \quad (1)$$

where the sum is over all other modes j within the bandwidth of the pulse, ω_{Aj} is the difference frequency between modes A and j, and θ_{Aj} is the angle between the transition dipole moments. The last term in the sum accounts for orientational ensemble averaging for parallel pump and probe

polarizations.[60] Since the action experiments are insensitive to population relaxation dynamics, Eq. 1 does not include exponential decay dynamics during τ_2. We note that the secular approximation does not include coherence transfer pathways.

Dynamics of Cross Peak Features. There are three pathways that give rise to off-diagonal cross peak bleach features between a pair of modes A and B under the secular approximation. Two of these pathways (one rephasing, one nonrephasing) are constant in the absence of population relaxation dynamics. The third pathway is a rephasing quantum beating pathway between modes A and B. Therefore, the signal for a cross peak bleach AB at (ω_1, ω_3) = (ω_A, ω_B) will evolve as:

$$\text{Signal}_{AB}(\tau_2) \propto |\mu_{A0}|^2|\mu_{B0}|^2 e^{-i\omega_{AB}\tau_2}\left(\frac{1}{15}(1+2\cos^2(\theta_{AB}))\right) \quad (2)$$

Unlike diagonal features, cross peaks only oscillate at a single difference frequency ω_{AB} during the pump-probe waiting time under the secular approximation.

Comparison of Experimental and Simulated Dynamics. In Fig. 2, we compare the experimental 2D IR spectra at 150 fs and 2000 fs waiting times to the simulated spectra obtained using Eqs. 1 and 2 under the secular approximation to nonlinear response theories. The squares of the transition dipole moments were taken from the integrated intensities of each peak in the experimental linear spectrum (Fig. 1b) and values of θ_{jk} were determined from the transition dipole moment vectors computed along the normal modes obtained in the harmonic approximation. Further details on the simulations can be found in SI. The simulated spectra reasonably capture the general diagonal and off-diagonal features of the experimental spectra. All spectra in Fig. 2 are absolute value absorptive spectra (sum of the rephasing and nonrephasing contributions). Real and absolute value spectra of the rephasing, nonrephasing, and absorptive signals are presented in Figs. S3-S6.

For a more in-depth analysis, we compare the time evolution of the experimental vs. simulated integrated intensities of the diagonal features in Fig. 3. Figure 3a shows the simulated absorptive dynamics for modes 1-6 computed with Eq. 1. Due to the multitude of oscillatory quantum beating pathways contributing to Eq. 1, the waiting time dynamics of the diagonal features are quite complicated. Figure 3b presents the experimental dynamics from the absorptive 2D IR spectra. Several key observations can be made from the comparison. First, as expected, the experimental dynamics show no indication of population relaxation or transfer (i.e., exponential decay dynamics). This is evidenced by experimental intensities that are larger at 1000 fs and 2000 fs compared to the two earlier waiting times for most modes, consistent with the simulations. In the absence of population relaxation, the single mode pathways contribute constant signals. The non-constant time evolution of the features, therefore, provides evidence that two-mode quantum beating pathways are major contributors to the spectral dynamics.

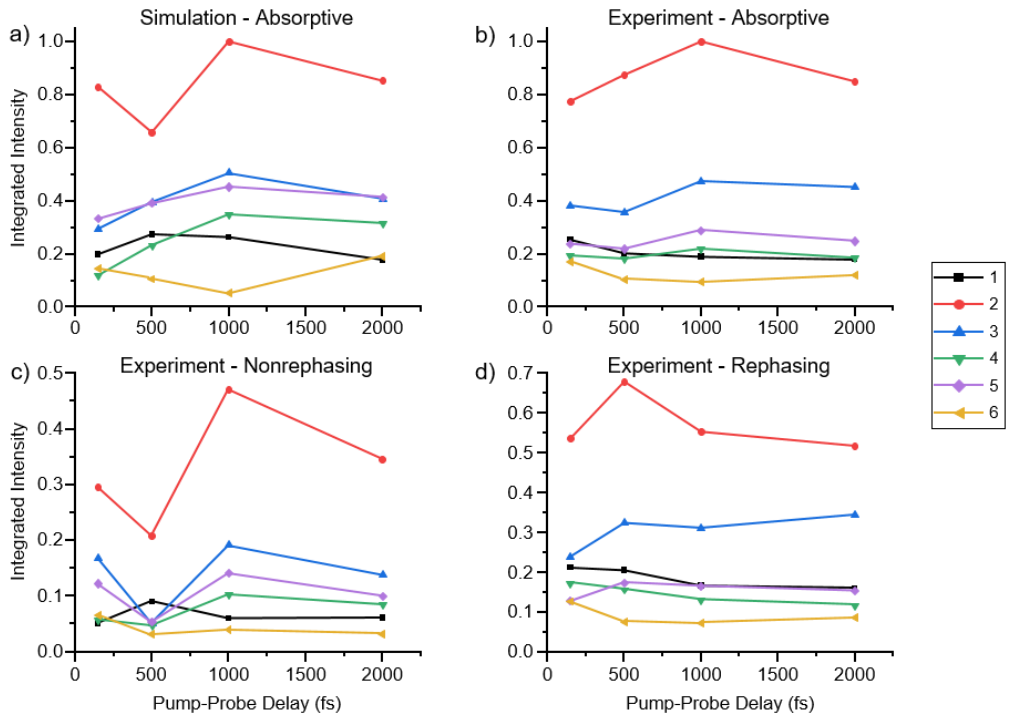

Fig. 3. Diagonal bleach dynamics for the six excited GSH vibrational modes from absolute value 2D IR spectra. (a) Simulated absorptive dynamics. (b) Experimental absorptive dynamics. (c) Experimental nonrephasing dynamics. (d) Experimental rephasing dynamics. Only oscillatory nonrephasing pathways should be present for diagonal features under the secular approximation.

Importantly, the experimental dynamics in Fig. 3b deviate significantly from those simulated in Fig. 3a, suggesting the presence of additional competing nonsecular pathways that are not accounted for in Eq. 1 due to coherence transfer processes. The experimental nonrephasing dynamics are shown in Fig. 3c. Since only nonrephasing pathways contribute to quantum beating pathways in the secular approximation, the nonrephasing signal is equal to the difference between the absorptive signal and the constant rephasing contribution. That is, the nonrephasing and absorptive oscillatory dynamics should be identical under the secular approximation. We, therefore, we do not show the simulated nonrephasing or constant rephasing dynamics in Fig. 3. Looking first at the strongest signal from mode 2 (red traces), the experimental nonrephasing dynamics are qualitatively captured by the simulated absorptive dynamics. The experimental absorptive dynamics of mode 2, however, differs significantly from the simulated dynamics. This is due to the non-constant contributions from the rephasing signal (Fig. 3d) that are not predicted under the secular approximation. Coherence transfer introduces new pathways that result in oscillatory rephasing quantum beating signals along the diagonal.[24–26,44] The experimental rephasing dynamics in Fig. 3d show clear intensity modulations for all modes that are not anticipated under the secular approximation, similar to the observations made by Guerrieri et al in ethylene carbonate.[26] The other vibrational modes exhibit stronger deviations between the experimental nonrephasing dynamics and simulated absorptive dynamics. Coherence transfer

during the pump-probe delay τ_2 from $|A\rangle\langle B|$ to $|A\rangle\langle C|$, for example, would change the relative contributions of the oscillatory components within the sum in Eq. 1, leading to deviations in the observed nonrephasing dynamics.

While there are many oscillatory contributions to the diagonal features, the cross peak features only contain one oscillatory component under the secular approximation (Eq. 2), simplifying spectral analysis. In Fig. 4, we compare the experimental and simulated cross peak dynamics involving mode 2. We analyze mode 2 cross peaks because they exhibit the strongest signals; analysis of the other weaker cross peak signals is challenging due to the lower signal-to-noise ratios. Figure 4a shows the simulated absorptive cross peak dynamics, with the experimental absorptive, rephasing, and nonrephasing dynamics presented in Figs. 4b, 4c, and 4d, respectively. The plotted signals are the sum of the lower and upper cross peak pairs. In contrast to diagonal features in the secular approximation, cross peaks dynamics are driven by the rephasing signal evolving at a single frequency ω_{AB}. Therefore, the experimental rephasing and absorptive cross peak dynamics should be the same, while the nonrephasing cross peak dynamics should be constant. For these reasons, we do not show the simulated rephasing and nonrephasing dynamics in Fig. 4.

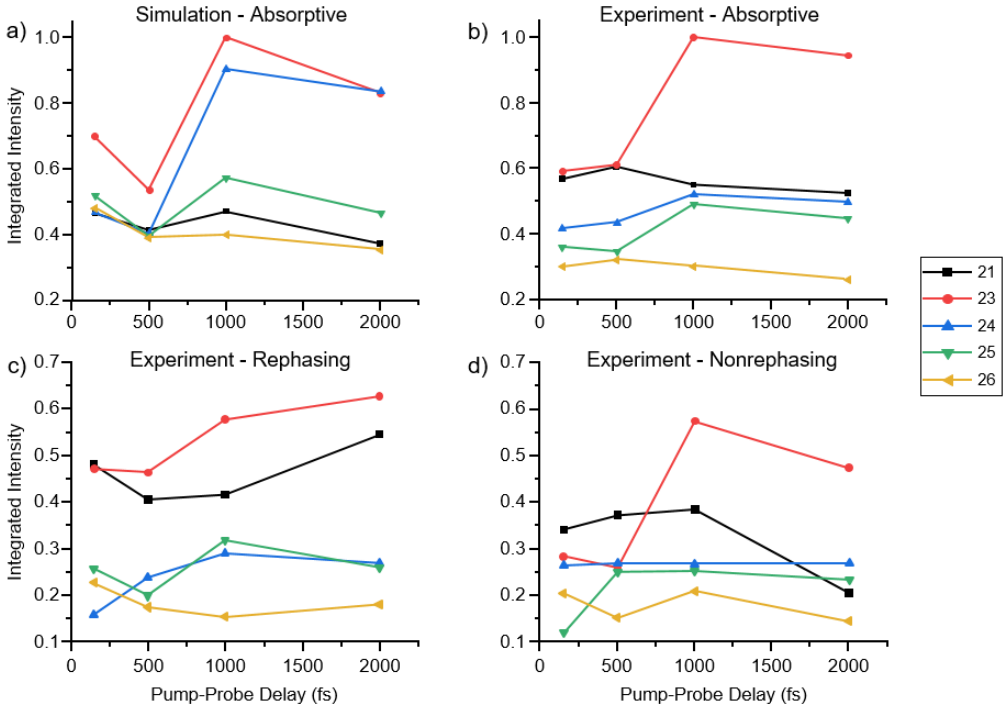

Fig. 4. Cross peak bleach dynamics involving vibrational mode 2 in GSH from absolute value 2D IR spectra. (a) Simulated absorptive dynamics. (b) Experimental absorptive dynamics. (c) Experimental rephasing dynamics. (d) Experimental nonrephasing dynamics. Only oscillatory rephasing pathways should be present for cross peak features under the secular approximation. The plotted intensities are the sum of the lower and upper cross peak signals.

In comparing the experimental rephasing dynamics (Fig. 4c), cross peak modes 2-5 and 2-6 show qualitative agreement with the simulated absorptive dynamics (Fig. 4a). The dynamics of the other three cross peak pairs, however, deviate significantly from the simulations. We attribute these deviations from the secular approximation to the presence of coherence transfer processes. For example, coherence transfer during τ_2 from $|A\rangle\langle B|$ to $|A\rangle\langle C|$ would introduce a new oscillatory component at frequency ω_{AC} to the rephasing signal. Previous condensed-phase studies have relied on the presence of multiple oscillatory components in cross peak rephasing signals to identify coherence transfer.[24,26,44] Coherence transfer would also introduce oscillatory nonrephasing quantum beating pathways onto off-diagonal positions that are not included under the secular approximation.[25,44] With the exception of cross peak mode 2-4, the nonrephasing cross peak signals (Fig. 4d) exhibit large signal fluctuations from constant as a function of the pump-probe waiting time, providing further evidence for the presence of coherence transfer pathways. The major deviations in relative intensity and dynamics indicate a multitude of nonsecular pathways that are giving rise to the complicated observed cross peak dynamics.

Coherence Transfer Pathways and Anharmonic Coupling. Coherence transfer events can occur during any of the three experimental waiting times (τ_1, τ_2, τ_3) and between any of the six transitions in GSH accessible within the bandwidth of the laser pulses. In SI, we list all possible nonsecular pathways that involve a single coherence transfer event in a three-mode system. In this scenario, 38 coherence transfer pathways can contribute to each diagonal peak (compared to just six secular pathways) and 33 pathways can contribute to cross peaks (compared to only three secular pathways). As detailed above and in SI, coherence transfer introduces new quantum beating pathways onto the diagonal and off-diagonal positions that are not predicted within the secular approximation. In addition, coherence-to-population and population-to-coherence pathways would cause further deviations from the expected signal intensities under the secular approximation.[25,26]

To determine if coherence transfer events are plausible between the six excited modes within the amide I-II region in GSH, we computed anharmonic cubic coupling constants using the VPT2 method. Table 1 reports the cubic coupling constants F_{jjk} and F_{jkk} between each pair of the six excited modes j and k. We also report cubic coupling constants F_{bbk} between the excited modes k and several low-frequency modes b. We anticipate that coupling is mediated between overtone and combination bands of the low-frequency modes with the excited modes represented by F_{bbk}. There are large (>30 cm^{-1}) cubic coupling constants predicted between the excited modes indicating significant anharmonic coupling exists between the amide I-II modes in GSH. More importantly, all six excited modes exhibit large coupling constants to low-frequency modes that can be categorized into four general families: $–NH_3^+$ hindered rotation (~400 cm^{-1}), NH wagging (~500 cm^{-1}), $–NH_3^+$ rocking (~1100 cm^{-1}), and more delocalized backbone modes (~1200 cm^{-1}). Displacement vectors for these low-frequency modes are provided in Fig. S7. In the absence of solvent, the low-frequency vibrational motions act as the bath. System-bath interactions mediate

coherence transfer through the coupling of the excited modes via mutual bath modes.[22,25,26,44] The shared coupling of the excited modes to a wide range of low-frequency bath modes indicates that coherence transfer processes are likely to occur in isolated GSH molecules. The strong anharmonic coupling to bath modes involving motions of the $–NH_3^+$ group, in particular, suggests that coherence transfer is driven by and mediated through the internal hydrogen bonds involving the $–NH_3^+$ group, similar to vibrational relaxation that occurs through the hydrogen bond network in model β-sheets.[16]

Table 1. Calculated VPT2 anharmonic cubic coupling constants (in cm^{-1}) for GSH. Coupling constants between the excited modes (1-6) are the F_{jjk} and F_{jkk} cubic terms (row j, column k). Coupling constants between the excited modes and low-frequency bath modes, b, are the F_{bbk} cubic terms. Calculations were performed at the ωB97X-D/6-31G(d) level and basis.

Mode	1	2	3	4	5	6
1		-33	-8	14	22	2
2	75		0	20	39	8
3	-33	-9		-16	-14	-44
4	-32	-30	-30		104	91
5	-19	-81	-50	10		-64
6	-10	-40	-78	80	218	
NH_3^+ rotation, 338 cm^{-1}	-158	-67	21	-44	17	28
NH_3^+ rotation, 390 cm^{-1}	-38	-17	-1	-48	5	5
NH wag, 470 cm^{-1}	-32	22	-4	-16	-50	-12
NH wag, 520 cm^{-1}	-16	-3	-34	-28	34	-45
NH_3^+ rock, 1152 cm^{-1}	-12	4	-2	-17	-20	-5
NH_3^+ rock, 1179 cm^{-1}	-10	-32	8	-31	-5	3
NH_3^+ rock, 1190 cm^{-1}	-31	-18	1	-36	0	11
backbone, 1129 cm^{-1}	5	-1	31	-8	4	-13
backbone, 1274 cm^{-1}	-8	3	-27	-14	16	-39
backbone, 1320 cm^{-1}	-24	30	-1	-5	-21	-10

Summary and Conclusions

Action 2D IR spectra of protonated GSH molecules isolated in the gas phase have been presented and analyzed in the context of the secular interaction pathways typically employed in nonlinear spectroscopies. The absence of excited-state features in action 2D IR allows for enhanced spectral resolution in congested regions and, importantly, the isolation of coherent quantum beating pathways from population relaxation dynamics. Action 2D IR spectroscopy of gas-phase molecules, therefore, provides an experimental platform to directly study coherent vibrational dynamics. Deviations in the measured spectral dynamics in GSH from those expected from the standard secular nonlinear response pathways indicate the presence of coherence transfer processes between the excited amide I-II vibrational modes, mediated through strong anharmonic

coupling with a large background of low-frequency bath modes. Although the limited set of spectra and multitude of possible nonsecular pathways do not allow us to identify the specific coherence transfer pathways present in GSH, the data demonstrate the presence of long-lived quantum beating dynamics that are likely to be prevalent energy transfer pathways within molecular and biological systems. Modeling vibrational energy relaxation dynamics in complex systems like peptides has largely relied on classical dynamical approaches, which do not accurately model population relaxation dynamics and do not consider coherent dynamics. Quantum dynamical approaches will be necessary to fully disentangle competing vibrational relaxation dynamics and pathways. More comprehensive experimental and theoretical investigations into coherence transfer dynamics will improve fundamental understanding and computational modeling of system-bath interactions in open quantum systems.

Supporting Information

Further experimental and data processing procedures, description of the configurational search procedure, traditional and action 2D IR Feynman diagrams, details on 2D IR simulations, Feynman diagrams for possible coherence transfer pathways for a model three-state system, and coordinates for the optimized geometry of GSH. Normal mode displacement vectors of the six excited modes within the laser pulse bandwidth (Fig. S1). 2D IR spectra of GSH at 500 fs and 1000 fs pump-probe waiting times (Fig. S2). Real and absolute value rephasing, nonrephasing, and absorptive 2D IR spectra at each collected waiting time (Figs. S3-S6). Normal mode displacement vectors of the most strongly coupled low-frequency bath modes (Fig. S7).

Acknowledgments

J.A.F. gratefully acknowledges support from NSF through a CAREER Award (Grant CHE-2044927). L.M.M. was supported by the Gas Phase Chemical Physics Program in the Division of Chemical Sciences, Geosciences and Biosciences, Office of Basic Energy Sciences (BES), U.S. Department of Energy (DOE). Sandia National Laboratories is a multi-mission laboratory managed and operated by National Technology Engineering Solutions of Sandia, LLC (NTESS), a wholly owned subsidiary of Honeywell International Inc., for the U.S. Department of Energy's National Nuclear Security Administration (DOE/NNSA) under contract DE-NA0003525. This written work is co-authored by an employee of NTESS. The employee, not NTESS, owns the right, title and interest in and to the written work and is responsible for its contents. Any subjective views or opinions that might be expressed in the written work do not necessarily represent the views of the U.S. Government. The publisher acknowledges that the U.S. Government retains a non-exclusive, paid-up, irrevocable, world-wide license to publish or reproduce the published form of this written work or allow others to do so, for U.S. Government

purposes. The DOE will provide public access to results of federally sponsored research in accordance with the DOE Public Access Plan.

Notes

The authors declare no competing financial interest.

References

(1) Baiz, C. R.; Błasiak, B.; Bredenbeck, J.; Cho, M.; Choi, J.-H.; Corcelli, S. A.; Dijkstra, A. G.; Feng, C.-J.; Garrett-Roe, S.; Ge, N.-H.; et al. Vibrational Spectroscopic Map, Vibrational Spectroscopy, and Intermolecular Interaction. *Chem. Rev.* **2020**, *120*, 7152–7218. DOI: 10.1021/acs.chemrev.9b00813.

(2) Jonas, D. M. Two-Dimensional Femtosecond Spectroscopy. *Annu. Rev. Phys. Chem.* **2003**, *54*, 425–463. DOI: 10.1146/annurev.physchem.54.011002.103907.

(3) Mukamel, S. *Principles of Nonlinear Optical Spectroscopy*; Oxford University Press: New York, 1995.

(4) Cho, M. Coherent Two-Dimensional Optical Spectroscopy. *Chem. Rev.* **2008**, *108*, 1331–1418. DOI: 10.1021/cr078377b.

(5) Biswas, S.; Kim, J.; Zhang, X.; Scholes, G. D. Coherent Two-Dimensional and Broadband Electronic Spectroscopies. *Chem. Rev.* **2022**, *122*, 4257–4321. DOI: 10.1021/acs.chemrev.1c00623.

(6) Hamm, P.; Zanni, M. *Concepts and Methods of 2D Infrared Spectroscopy*; Cambridge University Press: Cambridge, 2011.

(7) Redfield, A. G. The Theory of Relaxation Processes. In *Advances in Magnetic and Optical Resonance*; Waugh, J. S., Ed.; Advances in Magnetic Resonance; Academic Press, 1965; Vol. 1, pp 1–32. DOI: 10.1016/B978-1-4832-3114-3.50007-6.

(8) Kubo, R. A Stochastic Theory of Line Shape. *Adv. Chem. Phys.* **1969**, *15*, 101–127. DOI: 10.1002/9780470143605.ch6.

(9) Zhang, W. M.; Meier, T.; Chernyak, V.; Mukamel, S. Exciton-Migration and Three-Pulse Femtosecond Optical Spectroscopies of Photosynthetic Antenna Complexes. *J. Chem. Phys.* **1998**, *108*, 7763–7774. DOI: 10.1063/1.476212.

(10) Zhang, W. M.; Chernyak, V.; Mukamel, S. Multidimensional Femtosecond Correlation Spectroscopies of Electronic and Vibrational Excitons. *J. Chem. Phys.* **1999**, *110*, 5011–5028. DOI: 10.1063/1.478400.

(11) Roy, S.; C. Jansen, T. L.; Knoester, J. Structural Classification of the Amide I Sites of a β-Hairpin with Isotope Label 2DIR Spectroscopy. *Phys. Chem. Chem. Phys.* **2010**, *12*, 9347–9357. DOI: 10.1039/B925645H.

(12) Chung, H. S.; Ganim, Z.; Jones, K. C.; Tokmakoff, A. Transient 2D IR Spectroscopy of Ubiquitin Unfolding Dynamics. *Proc. Natl. Acad. Sci. U.S.A.* **2007**, *104*, 14237–14242. DOI: 10.1073/pnas.0700959104.

(13) Botan, V.; Backus, E. H. G.; Pfister, R.; Moretto, A.; Crisma, M.; Toniolo, C.; Nguyen, P. H.; Stock, G.; Hamm, P. Energy Transport in Peptide Helices. *Proc. Natl. Acad. Sci. U.S.A.* **2007**, *104*, 12749–12754. DOI: 10.1073/pnas.0701762104.

(14) Backus, E. H. G.; Bloem, R.; Donaldson, P. M.; Ihalainen, J. A.; Pfister, R.; Paoli, B.; Caflisch, A.; Hamm, P. 2D-IR Study of a Photoswitchable Isotope-Labeled α-Helix. *J. Phys. Chem. B* **2010**, *114*, 3735–3740. DOI: 10.1021/jp911849n.

(15) Mizutani, Y.; Mizuno, M. Time-Resolved Spectroscopic Mapping of Vibrational Energy Flow in Proteins: Understanding Thermal Diffusion at the Nanoscale. *J. Chem. Phys.* **2022**, *157*, 240901. DOI: 10.1063/5.0116734.
(16) Deniz, E.; Valiño-Borau, L.; Löffler, J. G.; Eberl, K. B.; Gulzar, A.; Wolf, S.; Durkin, P. M.; Kaml, R.; Budisa, N.; Stock, G.; et al. Through Bonds or Contacts? Mapping Protein Vibrational Energy Transfer Using Non-Canonical Amino Acids. *Nat. Commun.* **2021**, *12*, 3284. DOI: 10.1038/s41467-021-23591-1.
(17) Rubtsov, I. V.; Burin, A. L. Ballistic and Diffusive Vibrational Energy Transport in Molecules. *J. Chem. Phys.* **2019**, *150*, 020901. DOI: 10.1063/1.5055670.
(18) Rubtsova, N. I.; Rubtsov, I. V. Vibrational Energy Transport in Molecules Studied by Relaxation-Assisted Two-Dimensional Infrared Spectroscopy. *Annu. Rev. Phys. Chem.* **2015**, *66*, 717–738. DOI: 10.1146/annurev-physchem-040214-121337.
(19) Nawagamuwage, S. U.; Qasim, L. N.; Zhou, X.; Leong, T. X.; Parshin, I. V.; Jayawickramarajah, J.; Burin, A. L.; Rubtsov, I. V. Competition of Several Energy-Transport Initiation Mechanisms Defines the Ballistic Transport Speed. *J. Phys. Chem. B* **2021**, *125*, 7546–7555. DOI: 10.1021/acs.jpcb.1c03986.
(20) He, X.; Yu, P.; Zhao, J.; Wang, J. Efficient Vibrational Energy Transfer through Covalent Bond in Indigo Carmine Revealed by Nonlinear IR Spectroscopy. *J. Phys. Chem. B* **2017**, *121*, 9411–9421. DOI: 10.1021/acs.jpcb.7b06766.
(21) Stock, G. Classical Simulation of Quantum Energy Flow in Biomolecules. *Phys. Rev. Lett.* **2009**, *102*, 118301. DOI: 10.1103/PhysRevLett.102.118301.
(22) Khalil, M.; Demirdoven, N.; Tokmakoff, A. Vibrational Coherence Transfer Characterized with Fourier-Transform 2D IR Spectroscopy. *J. Chem. Phys.* **2004**, *121*, 362–373. DOI: 10.1063/1.1756870.
(23) Elsaesser, T. Two-Dimensional Infrared Spectroscopy of Intermolecular Hydrogen Bonds in the Condensed Phase. *Acc. Chem. Res.* **2009**, *42*, 1220–1228. DOI: 10.1021/ar900006u.
(24) Nee, M. J.; Baiz, C. R.; Anna, J. M.; McCanne, R.; Kubarych, K. J. Multilevel Vibrational Coherence Transfer and Wavepacket Dynamics Probed with Multidimensional IR Spectroscopy. *J. Chem. Phys.* **2008**, *129*, 084503. DOI: 10.1063/1.2969900.
(25) Baiz, C. R.; Kubarych, K. J.; Geva, E. Molecular Theory and Simulation of Coherence Transfer in Metal Carbonyls and Its Signature on Multidimensional Infrared Spectra. *J. Phys. Chem. B* **2011**, *115*, 5322–5339. DOI: 10.1021/jp109357d.
(26) Guerrieri, L.; Hall, S.; Luther, B. M.; Krummel, A. T. Signatures of Coherent Vibrational Dynamics in Ethylene Carbonate. *J. Chem. Phys.* **2024**, *161*, 164504. DOI: 10.1063/5.0216515.
(27) Ma, F.; Romero, E.; Jones, M. R.; Novoderezhkin, V. I.; Van Grondelle, R. Both Electronic and Vibrational Coherences are Involved in Primary Electron Transfer in Bacterial Reaction Center. *Nat. Commun.* **2019**, *10*, 933. DOI: 10.1038/s41467-019-08751-8.
(28) Policht, V. R.; Niedringhaus, A.; Ogilvie, J. P. Characterization of Vibrational Coherence in Monomeric Bacteriochlorophyll a by Two-Dimensional Electronic Spectroscopy. *J. Phys. Chem. Lett.* **2018**, *9*, 6631–6637. DOI: 10.1021/acs.jpclett.8b02691.
(29) Chenu, A.; Scholes, G. D. Coherence in Energy Transfer and Photosynthesis. *Annu. Rev. Phys. Chem.* **2015**, *66*, 69–96. DOI: 10.1146/annurev-physchem-040214-121713.
(30) Engel, G. S.; Calhoun, T. R.; Read, E. L.; Ahn, T.-K.; Mančal, T.; Cheng, Y.-C.; Blankenship, R. E.; Fleming, G. R. Evidence for Wavelike Energy Transfer through Quantum Coherence in Photosynthetic Systems. *Nature* **2007**, *446* , 782–786. DOI: 10.1038/nature05678.
(31) Thyrhaug, E.; Tempelaar, R.; Alcocer, M. J. P.; Žídek, K.; Bína, D.; Knoester, J.; Jansen, T. L. C.; Zigmantas, D. Identification and Characterization of Diverse Coherences in the Fenna–Matthews–Olson Complex. *Nat. Chem.* **2018**, *10*, 780–786. DOI: 10.1038/s41557-018-0060-5.
(32) Panitchayangkoon, G.; Hayes, D.; Fransted, K. A.; Caram, J. R.; Harel, E.; Wen, J.; Blankenship, R. E.; Engel, G. S. Long-Lived Quantum Coherence in Photosynthetic Complexes at Physiological

Temperature. *Proc. Natl. Acad. Sci. U.S.A.* **2010**, *107*, 12766–12770. DOI: 10.1073/pnas.1005484107.
(33) Scholes, G. D.; Fleming, G. R.; Chen, L. X.; Aspuru-Guzik, A.; Buchleitner, A.; Coker, D. F.; Engel, G. S.; Van Grondelle, R.; Ishizaki, A.; Jonas, D. M.; et al. Using Coherence to Enhance Function in Chemical and Biophysical Systems. *Nature* **2017**, *543*, 647–656. DOI: 10.1038/nature21425.
(34) Fuller, F. D.; Pan, J.; Gelzinis, A.; Butkus, V.; Senlik, S. S.; Wilcox, D. E.; Yocum, C. F.; Valkunas, L.; Abramavicius, D.; Ogilvie, J. P. Vibronic Coherence in Oxygenic Photosynthesis. *Nat. Chem.* **2014**, *6*, 706–711. DOI: 10.1038/nchem.2005.
(35) Romero, E.; Augulis, R.; Novoderezhkin, V. I.; Ferretti, M.; Thieme, J.; Zigmantas, D.; Van Grondelle, R. Quantum Coherence in Photosynthesis for Efficient Solar-Energy Conversion. *Nat. Phys.* **2014**, *10*, 676–682. DOI: 10.1038/nphys3017.
(36) Souri, S.; Timmer, D.; Lünemann, D. C.; Hadilou, N.; Winte, K.; De Sio, A.; Esmann, M.; Curdt, F.; Winklhofer, M.; Anhäuser, S.; et al. Ultrafast Time-Domain Spectroscopy Reveals Coherent Vibronic Couplings upon Electronic Excitation in Crystalline Organic Thin Films. *J. Phys. Chem. Lett.* **2024**, *15*, 11170–11181. DOI: 10.1021/acs.jpclett.4c02711.
(37) Phelan, B. T.; Zhang, J.; Huang, G.-J.; Wu, Y.-L.; Zarea, M.; Young, R. M.; Wasielewski, M. R. Quantum Coherence Enhances Electron Transfer Rates to Two Equivalent Electron Acceptors. *J. Am. Chem. Soc.* **2019**, *141*, 12236–12239. DOI: 10.1021/jacs.9b06166.
(38) Casotto, A.; Rukin, P. S.; Fresch, E.; Prezzi, D.; Freddi, S.; Sangaletti, L.; Rozzi, C. A.; Collini, E.; Pagliara, S. Coherent Vibrations Promote Charge-Transfer across a Graphene-Based Interface. *J. Am. Chem. Soc.* **2024**, *146*, 14989–14999. DOI: 10.1021/jacs.3c12705.
(39) Moisanu, C. M.; Eckvahl, H. J.; Stern, C. L.; Wasielewski, M. R.; Dichtel, W. R. A Paired-Ion Framework Composed of Vanadyl Porphyrin Molecular Qubits Extends Spin Coherence Times. *J. Am. Chem. Soc.* **2024**, *146*, 28088–28094. DOI: 10.1021/jacs.4c07288.
(40) Ishii, W.; Fuki, M.; Bu Ali, E. M.; Sato, S.; Parmar, B.; Yamauchi, A.; Mulyadi, C. H.; Uji, M.; Medina Rivero, S.; Watanabe, G.; et al. Macrocyclic Parallel Dimer Showing Quantum Coherence of Quintet Multiexcitons at Room Temperature. *J. Am. Chem. Soc.* **2024**, *146*, 25527–25535. DOI: 10.1021/jacs.4c05677.
(41) Chicco, S.; Allodi, G.; Chiesa, A.; Garlatti, E.; Buch, C. D.; Santini, P.; De Renzi, R.; Piligkos, S.; Carretta, S. Proof-of-Concept Quantum Simulator Based on Molecular Spin Qudits. *J. Am. Chem. Soc.* **2024**, *146*, 1053–1061. DOI: 10.1021/jacs.3c12008.
(42) Pakoulev, A.V.; Rickard, M.A.; Mathew, N.A.; Kornau, K.M.; Wright, J. C. Frequency-Domain Time-Resolved Four Wave Mixing Spectroscopy of Vibrational Coherence Transfer with Single-Color Excitation. *J. Phys. Chem. A* **2008**, *112*, 6320–6329. DOI: 10.1021/jp711014h.
(43) Marroux, H. J. B.; Orr-Ewing, A. J. Distinguishing Population and Coherence Transfer Pathways in a Metal Dicarbonyl Complex Using Pulse-Shaped Two-Dimensional Infrared Spectroscopy. *J. Phys. Chem. B* **2016**, *120*, 4125–4130. DOI: 10.1021/acs.jpcb.6b02979.
(44) Eckert, P. A.; Kubarych, K. J. Vibrational Coherence Transfer Illuminates Dark Modes in Models of the FeFe Hydrogenase Active Site. *J. Chem. Phys.* **2019**, *151*, 054307. DOI: 10.1063/1.5111016.
(45) Ma, Z.; Chen, L.; Xu, C.; Fournier, J. A. Two-Dimensional Infrared Spectroscopy of Isolated Molecular Ions. *J. Phys. Chem. Lett.* **2023**, *14*, 9683–9689. DOI: 10.1021/acs.jpclett.3c02661.
(46) Chen, L.; Ma, Z.; Fournier, J. A. Ultrafast Transient Vibrational Action Spectroscopy of Cryogenically Cooled Ions. *J. Chem. Phys.* **2023**, *159*, 041101. DOI: 10.1063/5.0155490.
(47) Chen, L.; Dean, J. L. S.; Fournier, J. A. Time-Domain Vibrational Action Spectroscopy of Cryogenically Cooled, Messenger-Tagged Ions Using Ultrafast IR Pulses. *J. Phys. Chem. A* **2021**, *125*, 10235–10244. DOI: 10.1021/acs.jpca.1c01996.
(48) Neese, F.; Wennmohs, F.; Becker, U.; Riplinger, C. The ORCA Quantum Chemistry Program Package. *J. Chem. Phys.* **2020**, *152*, 224108. DOI: 10.1063/5.0004608.
(49) Barone, V. Anharmonic Vibrational Properties by a Fully Automated Second-Order Perturbative Approach. *J. Chem. Phys.* **2005**, *122*, 014108. DOI: 10.1063/1.1824881.

(50) Krylov, A. I.; Gill, P. M. W. Q-Chem: An Engine for Innovation. *WIREs Comput. Mol. Sci.* **2013**, *3*, 317–326. DOI: 10.1002/wcms.1122.
(51) Gregori, B.; Guidoni, L.; Chiavarino, B.; Scuderi, D.; Nicol, E.; Frison, G.; Fornarini, S.; Crestoni, M. E. Vibrational Signatures of S-Nitrosoglutathione as Gaseous, Protonated Species. *J. Phys. Chem. B* **2014**, *118*, 12371–12382. DOI: 10.1021/jp5072742.
(52) Bruder, L.; Bangert, U.; Binz, M.; Uhl, D.; Vexiau, R.; Bouloufa-Maafa, N.; Dulieu, O.; Stienkemeier, F. Coherent Multidimensional Spectroscopy of Dilute Gas-Phase Nanosystems. *Nat. Commun.* **2018**, *9*, 4823. DOI: 10.1038/s41467-018-07292-w.
(53) De, A. K.; Monahan, D.; Dawlaty, J. M.; Fleming, G. R. Two-Dimensional Fluorescence-Detected Coherent Spectroscopy with Absolute Phasing by Confocal Imaging of a Dynamic Grating and 27-Step Phase-Cycling. *J. Chem. Phys.* **2014**, *140*, 194201. DOI: 10.1063/1.4874697.
(54) Maly, P.; Brixner, T. Fluorescence-Detected Pump-Probe Spectroscopy. *Angew. Chem. Int. Ed.* **2021**, *60*, 18867–18875. DOI: 10.1002/anie.202102901.
(55) Woutersen, S.; Mu, Y.; Stock, G.; Hamm, P. Subpicosecond Conformational Dynamics of Small Peptides Probed by Two-Dimensional Vibrational Spectroscopy. *Proc. Natl. Acad. Sci. U.S.A.* **2001**, *98*, 11254–11258. DOI: 10.1073/pnas.201169498.
(56) Terry, L. M.; Klumb, M. K.; Nemchick, D. J.; Hodyss, R.; Maiwald, F.; Weber, J. M. Cryogenic Ion Vibrational Spectroscopy of Protonated Valine: Messenger Tag Effects. *J. Phys. Chem. A* **2024**, *128*, 7137–7144. DOI: 10.1021/acs.jpca.4c03552.
(57) Yoo, H. S.; DeWitt, M. J.; Pate, B. H. Vibrational Dynamics of Terminal Acetylenes: I. Comparison of the Intramolecular Vibrational Energy Redistribution Rate of Gases and the Total Relaxation Rate of Dilute Solutions at Room Temperature. *J. Phys. Chem. A* **2004**, *108*, 1348–1364. DOI: 10.1021/jp027543a.
(58) Yoo, H. S.; DeWitt, M. J.; Pate, B. H. Vibrational Dynamics of Terminal Acetylenes: II. Pathway for Vibrational Relaxation in Gas and Solution. *J. Phys. Chem. A* **2004**, *108*, 1365–1379. DOI: 10.1021/jp027546n.
(59) Yoo, H. S.; McWhorter, D. A.; Pate, B. H. Vibrational Dynamics of Terminal Acetylenes: III. Comparison of the Acetylenic C−H Stretch Intramolecular Vibrational-Energy Redistribution Rates in Ultracold Molecular Beams, Room-Temperature Gases, and Room-Temperature Dilute Solutions. *J. Phys. Chem. A* **2004**, *108*, 1380–1387. DOI: 10.1021/jp0275443.
(60) Hochstrasser, R. M. Two-Dimensional IR-Spectroscopy: Polarization Anisotropy Effects. *Chem. Phys.* **2001**, *266*, 273–284. DOI: 10.1016/S0301-0104(01)00232-4.